

Insights into the 3D structure and behaviour of Icelandic crystal mushes from gabbroic nodules

Rahul Subbaraman^{1,*}, Margaret E. Hartley¹, Jonathan Fellowes¹, Margherita Polacci¹, Barbara Bonechi¹, Lucia Pappalardo², Gianmarco Buono², David A. Neave¹

¹ Department of Earth and Environmental Sciences, University of Manchester, Oxford Road, Manchester, M13 9PL, UK

² Istituto Nazionale di Geofisica e Vulcanologia – Osservatorio Vesuviano, Via Diocleziano 328, 80125 Napoli, Italy

Corresponding author: Rahul Subbaraman

rahul.subbaraman@manchester.ac.uk

This peer-reviewed preprint has been submitted to EarthArXiv. It has completed peer review at *Earth and Planetary Science Letters*, but final acceptance and publication are pending. If accepted, the final version will be available from the publisher with a DOI.

© 2025. This preprint is made available under a
Creative Commons Attribution (CC BY 4.0) license.

Insights into the 3D structure and behaviour of Icelandic crystal mushes from gabbroic nodules

Rahul Subbaraman ^a, Margaret E. Hartley ^a, Jonathan Fellowes ^a, Margherita Polacci ^a, Barbara Bonechi ^a, Lucia Pappalardo ^b, Gianmarco Buono ^b, David A. Neave ^a

Department of Earth and Environmental Sciences, University of Manchester, Oxford Road, Manchester, M13 9PL, UK

Istituto Nazionale di Geofisica e Vulcanologia - Osservatorio Vesuviano - Sezione di Napoli, Via Diocleziano, 328, 80125, Napoli NA, Italy

Abstract

Crystal mushes – porous yet cohesive frameworks of crystals interspersed with interstitial melts – form the plumbing systems of active volcanoes. In Iceland, magmatic plumbing systems are inferred to be constructed from vertically stacked mushy magma reservoirs separated by subsolidus rock. Gabbroic nodules from Gígöldur in central Iceland provide a rare window into the structure, evolution, and degassing behaviour of upper crustal (6–10 km) mushy magma reservoirs. These plagioclase-rich nodules preserve recycled high-An plagioclase cores, rim overgrowths, and interstitial mafic crystallisation, reflecting *in situ* modification within the final storage reservoir and roof cumulate formation via density-driven segregation. Oscillatory zoning and variable rim patterns indicate that crystals experienced non-steady-state growth and were incorporated into clusters at different times. Compositional similarity between carrier and interstitial melts demonstrates that the final stages of mush evolution occurred in relatively homogeneous melts. Volatile saturation pressures of ~2.0–2.8 kbar, together with high vesicu-

larity (21–30 vol.%) and extensive connectivity (>93%), are consistent with the presence of a CO₂-rich vapour phase within the mush. Nodules are erupted when a rigid crystal framework and a well-connected bubble network, which enables effective degassing, preserve their integrity. Where bubble networks fail to form, degassing disrupts the framework – even if initially rigid – causing disaggregation into plagioclase-phyric crystal cargoes, akin to plagioclase-ultraphyric basalts erupted in diverse settings. Nodules record the dynamics of stratified mushy magma reservoirs, the influence of volatiles on mush behaviour, and the transport of crystalline material in active volcanic systems, providing new insights into how crystal mushes shape the storage and mobilisation of magma in the Earth’s crust.

Keywords: gabbroic nodules, crystal mush, magma plumbing system, plagioclase-rich cumulates, stratified magma reservoirs, Icelandic volcanism

1. Introduction

Active volcanoes are increasingly understood to be fed from geometrically complex transcrustal plumbing systems composed of crystal mushes – cohesive yet porous frameworks of crystals interspersed with interstitial melts (e.g., [Annen et al., 2005](#); [Edmonds et al., 2019](#)). Plumbing systems are often discussed in terms of two endmember architectures. In continental settings, they are typically described as largely continuous mush columns that extend through much of the crust (e.g., [Cashman et al., 2017](#); [Paulatto et al., 2019](#)), whereas in oceanic settings such as Iceland, plumbing systems are often depicted as stacked, localised mushy magma reservoirs dispersed through the crust but separated by melt-free country rock (e.g., [Chamberlain et al., 2019](#); [MacLennan, 2019](#)). In this stacked-sill configuration, mush zones form at the margins of individual sills emplaced

into subsolidus crust, reflecting localised rather than pervasive mush development (MacLennan, 2019). Examining the 3D pre- and syn-eruptive crystal mush textures can constrain the conditions and dynamics of magma storage, remobilisation, and ascent, thereby contributing to the refinement of magma behaviour models (e.g., Bergantz et al., 2015; Sparks and Cashman, 2017; Humphreys et al., 2025). However, this undertaking is extremely challenging. Mush-derived clots of crystals often disaggregate during magma ascent (e.g., Hansen and Grönvold, 2000; Holness et al., 2007; Lange et al., 2013), while mushes preserved in fossil magma reservoirs are subject to overprinting by post-emplacement physical and chemical processes (e.g., O'Driscoll et al., 2010; Holness et al., 2017). In this context, gabbroic nodules, also known as cognate xenoliths, plutonic nodules, or crystalline enclaves (Holness et al., 2019), provide a vital opportunity to investigate the petrology of mushy magma reservoirs beneath basaltic volcanoes. While numerous studies have explored the 2D structure of mush fragments and mush-derived crystal clusters in basalts (e.g., Neave et al., 2014b; Horn et al., 2022; Holness et al., 2019), analogous 3D studies remain to be undertaken. Such 3D imaging provides a more comprehensive view of nodule textures by capturing geometric and spatial relationships that are difficult (or sometimes impossible) to interpret from 2D sections alone. In particular, 3D data can reveal vesicle size distributions and connectivity – features that inform interpretations of degassing pathways and deformation history – as well as the spatial arrangement and interconnectivity of crystalline frameworks and interstitial phases. These insights are commonly obscured or misrepresented in 2D due to sectioning bias.

Constraining the distribution and behaviour of H₂O and CO₂ in crystal mushes

is essential to deciphering their degassing behaviour within magma plumbing systems and their influence on magma ascent and crystal mush disaggregation. Volatiles, whether dissolved in magma or exsolved as bubbles, critically influence magma dynamics and eruptive activity (e.g., [Edmonds and Wallace, 2017](#)). As volatiles exsolve, they form bubbles that, when preserved, become vesicles and provide vital clues about degassing processes. Studying vesicle textures is therefore a key approach to reconstructing volatile behaviour in magma systems. Advances in X-ray computed microtomography (XCT), pioneered by [Proussevitch et al. \(1998\)](#), have revolutionised vesicle studies, offering insights into outgassing dynamics, bubble coalescence, and magma ascent behaviour during eruptions. A deeper understanding of these processes improves our ability to interpret magma degassing pathways, pressure changes, and fragmentation dynamics. In turn, these factors directly influence eruption style, intensity, and timing ([Klug and Cashman, 1994](#); [Cashman and Mangan, 2014](#)), with direct implications for enhancing predictions of eruptive behaviour and informing volcanic hazard mitigation. Vesicle size distributions are widely used to infer nucleation, growth, and coalescence events during vesiculation ([Klug and Cashman, 1994](#)). X-ray computed microtomography analyses of volcanic samples from Ambrym (Vanuatu), Etna (Italy), Hunga Tonga–Hunga Ha’apa (Tonga), Las Sierras–Masaya (Nicaragua), Stromboli (Italy), and La Palma (Canary Islands, Spain) have demonstrated the utility of this technique in tracking vesicle connectivity and vesicle number density in pyroclasts ([Polacci et al., 2009, 2012](#); [Colombier et al., 2018](#); [Bamber et al., 2024](#); [Bonechi et al., 2025](#)). Vesicle connectivity provides a measure of gas escape efficiency through permeable bubble networks, while vesicle number density can reflect volatile nucleation and decompression rates. Together they offer critical insights into magma degassing,

ascent dynamics, and eruptive style, including whether magma undergoes explosive fragmentation or degasses passively (e.g., [Klug and Cashman, 1996](#); [Toramaru, 2006](#); [Shea et al., 2010](#)).

While XCT approaches are typically applied to eruptive products, applying the same principles to gabbroic nodules offers a unique opportunity to investigate degassing in a contrasting environment – one where a rigid crystal framework coexists with the exsolving volatile phase. Exsolved volatiles reduce magma density and aid ascent, but if bubble growth and overpressure are not efficiently relieved through gas or melt escape, they can generate stresses that cause nodule disaggregation, as observed in mafic enclaves within volcanic rocks (e.g., [Bacon, 1986](#); [Candela, 1991](#)). Understanding mush disaggregation also raises important questions about how crystal mush fragments become entrained, transported and preserved during magma ascent. The detachment of such fragments, likely driven by fracturing and dislodgement from their source regions, remains poorly understood ([Holness et al., 2019](#)). To survive transport without breaking down into isolated macrocrysts (e.g., [Hansen and Grönvold, 2000](#); [Lange et al., 2013](#); [Neave et al., 2014b](#)), entrained mush fragments must retain sufficient structural integrity. Most erupted nodules contain >60 vol.% crystals and <30 vol.% vesicles ([Holness et al., 2019](#)), reflecting the minimum crystal fraction required to form a mechanically stable framework and the weakening effects of increasing vesicularity ([Coombs et al., 2003](#)).

Here, we focus on exceptionally well-preserved gabbroic nodules from Gígöldur in central Iceland, first reported by [Hansen and Grönvold \(2000\)](#). We use these

nodules to address two key questions: (1) What do gabbroic nodules reveal about crystal mush texture and chemistry at depth? (2) How well do the gabbroic nodules retain structural integrity during ascent? By addressing these questions, we show that gabbroic nodules provide a valuable archive for reconstructing mush dynamics and disaggregation processes, offering insights into how such processes influence magma storage and eruption in volcanic systems globally.

2. Samples and analytical methods

Gígöldur is a broad NNE-SSW-trending ridge of interlayered hyaloclastites and craters situated in the highlands north of Vatnajökull glacier, located between Bárðarbunga to the southwest and Askja to the northeast (Figure 1a; Hansen and Grönvold, 2000). Nodule samples were collected from two locations along the ridge, approximately 5 km apart, referred to as Gígöldur Central and Gígöldur South (Figure 1b,c). The nodules are 5-10 cm in diameter, rounded to sub-angular, and composed mainly of plagioclase aggregates encased in glass. They also contain small but variable amounts of interstitial olivine, and interstitial dark green clinopyroxene is present in some nodules. They exhibit high vesicularity and significant textural and mineralogical variability (Figure 1d). While most nodules were picked up loose from the float, some nodules were found *in situ* within plagioclase-phyric scoriaceous agglutinates (Figure 1e,f).

A summary of samples analysed in this study, including sample types and the analytical techniques used, is provided in Supplementary Table B1. Two nodules (GO19-01a.X and GO19-02.X), each about 10 cm in their longest dimension (Figure 1g) but relatively thin (~3 cm), were selected for further investigation because

their thin geometries allowed the XCT scan cores to encompass a substantial proportion of the total nodule volumes. Four cylindrical rock cores were drilled from each nodule ([Figure 1h](#)). The cores are 15 mm in diameter and 16.7 to 27.5 mm in height to accommodate variations in nodule morphologies while maintaining sample integrity. Cores from sample GO19-01a.X were designated Batch I, and those from GO19-02.X were designated Batch II, corresponding to their nodule of origin. Because the two samples responded differently to X-ray exposure, different exposure times were required, which in turn necessitated slightly different segmentation strategies. A total of seven thin sections were prepared from areas between the cores of both nodules.

Plane-polarised light (PPL) images were captured at a high resolution of 5000 pixels per inch using a GX Microscopes PrimeScan system. Partial-XPL (PXPL; polariser–analyser 45°) and XPL (90°) images were acquired at ×10 magnification using a uScope GX-1020 Geological Slide Scanner; the PXPL setup avoids complete extinction of silicate phases across the thin section. Phase proportions were quantified through a modified point-counting method using the image analysis software JMicroVision v. 1.3.4 ([Roduit, 2008](#)). PPL or PXPL images of the thin sections were systematically segmented into equal-area rectangles. Successive grids were generated by subdividing the initial grid at its midpoints, enabling a detailed assessment of mineral distribution and precise quantification of all constituent phases across the thin sections.

X-ray computed microtomography (XCT) was performed using a Carl Zeiss Xradia Versa-410 3D X-ray microscope at the Istituto Nazionale di Geofisica e Vul-

canologia - Sezione di Napoli Osservatorio Vesuviano (INGV-OV), Naples, Italy. Scans were performed in absorption mode with 1601 projections collected over a 360° rotation at 90 kV and 8 W, and an optical magnification of $\times 0.4$, resulting in a nominal voxel size of 16.0918 μm . Typical macrocrysts are $\geq 100 \mu\text{m}$ in length, and the smallest interstitial melt films between them are at least 20 μm thick, while most bubbles have minimum dimensions of $\geq 10 \mu\text{m}$. Thus, our voxel size is sufficient to resolve the textural features relevant to our goals. Data were reconstructed using XRMReconstructor, and vesicle and crystal geometries were characterised and quantified using Thermo Scientific™ Avizo v. 2019.1 and Fiji v1.54f. Details of the XCT analysis methods are provided in the supplementary material. Our XCT analysis aimed to distinguish constituent phases – plagioclase, olivine, clinopyroxene, matrix glass, and vesicles – using a lab-based XCT setup. However, since we used absorption contrast mode and prioritised glass-plagioclase separation, olivine and clinopyroxene could not be distinguished in Batch I, necessitating their combined classification as mafics in subsequent analyses and discussions.

Minerals and glasses were geochemically characterised in one representative thin section from each of the scanned nodules (GO19-01a.6 and GO19-02.4; Supplementary Table B1). These thin sections were selected to minimise the presence of ash within vesicles (to avoid complications in density calculations) while ensuring that all major phases were included. Additional mineral analyses were conducted on five additional nodule thin sections and three scoria thin sections, representing different sampling locations and textures to capture mineralogical variability. Glass analyses were performed on four nodule and two scoria thin sections from this set. Major and minor element compositions of minerals and interstitial glass

were determined by electron probe microanalysis (EPMA) on a Cameca SX100 instrument at the Williamson Research Centre, University of Manchester. Analyses were performed under typical operating conditions of 15 kV accelerating voltage, 5–40 nA beam current, and 1–10 μm beam diameter, with counting times of 20–60 s on-peak and 10–30 s off-peak depending on the phase. Accuracy and precision were monitored using secondary standards. Detection limits for individual oxides were typically: SiO_2 , MgO , FeO , Al_2O_3 , CaO $\sim 0.03\text{--}0.04$ wt%; MnO , TiO_2 , NiO $\sim 0.04\text{--}0.06$ wt%; and Cr_2O_3 , Na_2O , K_2O , P_2O_5 $\sim 0.01\text{--}0.02$ wt%. Full details of the analytical setup, standard measurements, and instrument configurations are provided in the supplementary material.

Magmatic H_2O concentrations were reconstructed from published melt inclusion data. We compiled clinopyroxene-hosted, olivine-hosted, and plagioclase-hosted melt inclusions from Holuhraun (Bali et al., 2018), together with olivine-hosted inclusions from Skuggafjöll (Neave et al., 2014b), comprising a total of 209 melt inclusions (see supplementary material). These eruptions were chosen for their geochemical similarity and geographic proximity to Gígöldur (Supplementary Figure B1). Because Ce data (commonly used as a proxy for H_2O under H_2O -undersaturated conditions) are unavailable for Gígöldur, H_2O concentrations were inferred by exploiting the similarity in median $\text{H}_2\text{O}/\text{MgO}$ values within the compiled dataset (Supplementary Figure B2).

Plausible CO_2 concentrations were reconstructed from maximum CO_2/Ba ratios in a dataset comprising 336 clinopyroxene-hosted, olivine-hosted, and plagioclase-hosted melt inclusions from Borgarhraun, Holuhraun, and Skuggafjöll (Supple-

mentary Table B4; full data in the supplementary material; [Hauri et al., 2017](#); [Bali et al., 2018](#); [Neave et al., 2014a](#)). CO₂/Ba ratios were converted to CO₂ concentrations using the Ba content of Gígöldur nodule glass (19 ppm; [Hansen and Grönvold, 2000](#)). For each locality and host phase, *realistic maximum* CO₂ values were calculated using the Tukey upper bound ($Q3 + 1.5 \times IQR$; [Tukey, 1977](#)) of the CO₂/Ba distributions to provide conservative upper limits while minimising the influence of extreme outliers.

Storage conditions were constrained with the empirical olivine–plagioclase–augite–melt (OPAM) thermobarometer of [Higgins and Stock \(2024\)](#), which applies a multivariate regression to melt major element chemistry (matrix glasses here) and a statistical filter that evaluates the probability of OPAM saturation. We retain only high-probability OPAM-saturated solutions (low-probability/edge-of-calibration cases are rejected; thresholding details in [Higgins and Stock, 2024](#)). The calibration yields standard errors of ± 1.14 kbar and ± 36 °C, with low systematic uncertainties that are independent of melt H₂O.

Bulk nodule densities were determined by combining modal mineral proportions from point counting with mineral and interstitial melt densities, both calculated at the inferred storage P–T condition. Melt densities were obtained using a partial molar volume approach following [Lange and Carmichael \(1990\)](#), in which oxide contributions vary with pressure and temperature. Mineral densities were calculated from their endmember compositions and the thermoelastic formulation of [Berman \(1988\)](#), which accounts for P–T effects on molar volumes. To assess the buoyancy of the nodules, carrier melt (scoria matrix glass) densities were also

calculated at the same P–T. The procedures for liquid and mineral density calculations, including the equations and thermodynamic parameters used, are detailed in the supplementary material, and the Python code is available at [Subbaraman \(2025\)](#).

3. Results

3.1. Petrography and point counting

Point counting (3400 points per section) shows that the nodules are strongly plagioclase-dominated (50–64 vol%). Olivine ranges from 0.7–4.2 vol% when clinopyroxene is present (2.8–9.8 vol%) and 1.9–8.5 vol% when it is absent. Interstitial glass makes up 8.6–20.7 vol%, and vesicles 16–25 vol% ([Figure 2a](#)). These proportions place the nodules within the IUGS fields of anorthosite, leuco-troctolite, and leucogabbro ([Figure 2b](#)). All samples contain plagioclase, olivine, glass, and vesicles; clinopyroxene is restricted to GO19-01a.X and GO19-01a.1. Accessory Cr-spinel occurs in GO19-02.X, GO19-01a.1, GO19-01a.3, and GO23-04.N3C, while particulate volcanic ash is confined to vesicle cavities and margins in GO19-02.2. Full thin section photomicrographs are provided in [Figure 3a–d](#).

Plagioclase grains (100 μm to >5 mm) primarily form clusters rather than isolated crystals and often host melt inclusions. XPL photomicrographs reveal multiple bands of rims enclosing both individual plagioclase crystals and clusters ([Figure 3e–j](#)). Olivine grains are typically smaller (<1.5 mm) and are found interstitially between plagioclase clusters, often in the vicinity of vesicles. Clinopyroxene, when present, is subhedral to sub-rounded, enclosed by plagioclase, and contains fractures and melt inclusions. Cr-spinel, when present, is associated with plagioclase

clase and olivine. Vesicles in all samples span a wide range of sizes and degrees of coalescence, from smaller (<0.2 mm) circular vesicles to larger (>1 mm) irregular vesicles that are partially or fully coalesced. They are commonly rimmed by glass of variable thickness. A full set of thin section scans is available in [Subbaraman et al. \(2025a\)](#).

3.2. *X-ray computed microtomography (XCT) analysis*

In Batch I, vesicles were readily segmented from surrounding glass and crystals using simple thresholding, complemented by image processing techniques in Avizo, including Erosion, Dilation, and Removal of Small Spots. Segmentation in Batch II was more challenging due to a few vesicles containing particulate volcanic ash, which may have caused a slight underestimation of vesicle abundance. Approximately 1 vol.% of pixels in Batch I and 4 vol.% in Batch II remain unassigned due to segmentation limitations. Individual plagioclase crystals show minimal phase contrast with neighbouring grains, so individual plagioclase grains within clusters could not be segmented in either batch. Volumetric proportions from XCT data are shown in [Figure 2a](#), with representative 3D renderings in [Figure 4a, b](#). A full set of reconstructions is available in [Subbaraman et al. \(2025b\)](#).

3.2.1. *Minerals and glasses*

Mineralogical diversity across the cores, highlighted through 3D visualisation, is detailed in Supplementary Table B3. Estimated volume proportions broadly agree with the point-counting results considering sectioning effects, and highlight systematic differences between the two nodules ([Figure 2a](#)). Batch I cores contain 55–60 vol% plagioclase, 4.7–10 vol% mafics, 5.3–9.2 vol% glass, and 25–30 vol% vesicles, whereas Batch II cores contains slightly less plagioclase (50–56 vol%),

fewer mafics (4.0–6.5 vol%), more glass (13–20 vol%), and vesicles (22–24 vol%). Accessory Cr-spinel (0.05–0.08 vol%) occurs only in Batch II. Mafic phases occupy interstitial spaces between plagioclase clusters, and are relatively larger and clustered in Batch I, and relatively smaller and more disseminated in Batch II. Apparent clustering of mafic phases most likely reflects the limited resolution of segmentation at grain boundaries. Coarse plagioclase grains in contact could not be reliably separated, precluding quantitative shape analysis.

3.2.2. Vesicles

After applying geometrical filters, 3D volume analysis reveals vesicle sizes spanning approximately $10^4 \mu\text{m}^3$ (the conservative lower detection limit imposed by the 16 μm voxel size) to over $10^{10} \mu\text{m}^3$ (Supplementary Table B4). Vesicles smaller than the minimum threshold may be present but cannot be robustly identified. Vesicle textures show consistent differences between the two batches, although variability within each batch is comparatively low. Batch I cores have a mean vesicle content of ~ 27 vol.%, while Batch II cores contain ~ 22.5 vol.% vesicles. Vesicle connectivity, defined as the volume fraction of interconnected vesicles extending to the core edges, is high across samples (93.3–98.8%; Supplementary Table B4; [Figure 4c](#)). Cores with the highest and lowest connectivity are highlighted in [Figure 4d](#), illustrating the range of vesicle network development. Vesicles larger than $10^6 \mu\text{m}^3$ (constituting $>99\%$ of the vesicle volume) are the main focus of subsequent analyses, as smaller vesicles likely formed during syn-eruptive vesiculation in shallow conduits ([Klug and Cashman, 1996](#)) and are not directly relevant to mush textures. Large vesicles instead record pre-eruptive bubble growth in magma chambers ([Sparks and Brazier, 1982](#)) or syn-eruptive coalescence ([Klug and Cashman, 1994](#)).

Vesicle populations exhibit three broad morphological styles that recur across cores: (i) nearly spherical to weakly ellipsoidal vesicles with little or no evidence of coalescence; (ii) sub-spherical to botryoidal vesicles; and (iii) large, irregular and tortuous vesicles formed by partial to extensive coalescence around the crystal framework. These morphologies are consistent with those reported from 2D vesicle textures, but are here fully resolved in 3D. For quantitative analysis, vesicle size distributions (VSDs) were fitted using fixed log-volume bins of 10^6 – 10^8 , 10^8 – 10^9 , and 10^9 – 10^{10} μm^3 (Supplementary Figure B3). This binning captures the natural breaks in the VSDs across all cores and allows direct comparison between batches. The smallest vesicles (10^6 – 10^8 μm^3) follow power-law distributions with exponents of 0.39–0.44 in Batch I and 0.64–0.74 in Batch II. Medium vesicles (10^8 – 10^9 μm^3) show power-law trends with exponents 1.04–1.19 in Batch I and 0.44–0.69 in Batch II. The largest vesicles (10^9 – 10^{10} μm^3) either follow steep power-law distributions with exponents 1.36–1.85 (Batch I) and 1.36–1.57 (Batch II) or exhibit exponential tails, as shown by the red curves and annotations in Supplementary Figure B2.

3.3. *Storage conditions and volatile contents*

Matrix glasses in all nodules and scoria samples are basaltic in composition (Supplementary Figure B3), with nodule matrix glasses chemically similar to scoria matrix glasses (Supplementary Figure B4). OPAM thermobarometry (Higgins and Stock, 2024) indicates that the most probable storage conditions were $\sim 2.45 \pm 1.14$ kbar and $1211 \pm 36^\circ\text{C}$ (Figure 5); calculated phase densities at these conditions reported in Table 1. Melt inclusion data from Holuhraun and Skuggafjöll, selected for their geochemical similarity to Gígöldur, indicate reconstructed H_2O concen-

trations of approximately 0.30–0.47 wt% (Supplementary Material), based on the observed best-fit linear correlation $\text{H}_2\text{O} = 0.0520 \times \text{MgO}$ (Supplementary Figure B2). For CO_2 , the literature compilation of 336 melt inclusions from Borgarhraun, Holuhraun, and Skuggafjöll yields maximum CO_2/Ba ratios of 79–115. Using the Ba content of Gígöldur nodule glass (19 ppm; [Hansen and Grönvold, 2000](#)), we estimate a realistic maximum CO_2 concentration of 1120–1350 ppm (Supplementary Table B4).

4. Discussion

4.1. *How well do the gabbroic nodules retain structural integrity during ascent?*

The absence of obvious fabrics, such as foliation or lineation ([Figure 3a-d](#)), together with the near-continuous nature of the plagioclase-dominated framework (~99% in contact), indicates that the crystal framework was stable during the eruption. Both 2D and 3D observations suggest that plagioclase grains are dominantly equant to sub-equant, i.e., of low aspect ratio. Indeed, such grain shapes are far less susceptible to bending or fracture during rapid vesicle expansion than tabular plagioclase ([Martin et al., 2006](#)). Moreover, the framework is marked by extensive grain-grain contacts ([Figure 3e,f,i](#)), consistent with other melt-bearing rocks potentially associated with synneusis where contact areas greatly exceed those predicted by equilibrium dihedral angles ([Holness et al., 2012](#)). Large contacts are widely recognised to enhance mush cohesion ([Holness, 2018](#)), providing mechanical robustness against disruption during vesicle growth, coalescence, or melt extraction. Taken together, the predominance of equant to sub-equant plagioclase grains and their extensive contact surfaces implies that the Gígöldur nodules developed a resilient framework capable of withstanding stresses associated with vesiculation and

degassing.

The potential for mush framework disruption is strongly influenced by bubble growth and coalescence. Bubble expansion exerts localised stresses on the surrounding crystal network, and extensive bubble coalescence can compromise framework integrity (e.g., [Coombs et al., 2003](#)). We observe high connectivity in both matrix glasses (>90%) and vesicles (>93%), which suggests that gas and melt could escape efficiently during the final stages of eruption. Vesicle size distributions ([Figure 6a,b](#), Supplementary Figure B3) provide further insights; vesicles exceeding $10^9 \mu\text{m}^3$ display high power-law exponents (>1), indicative of bubble coalescence facilitating the formation of interconnected degassing pathways (e.g., [Gaonac'h et al., 1996](#); [Bai et al., 2008](#)). Exponential fits in some cores (Supplementary Figure B3) suggest that degassing approached near-equilibrium conditions ([Bai et al., 2008](#)).

We modelled closed-system degassing profiles for CO_2 , H_2O , and total volatiles in 100 pressure decrements from the depth of final storage (1.67—3.00 kbar) to a confining pressure of 84.5 bar, corresponding to ~940 m of ice cover – the average in central Iceland during the Last Glacial Maximum ([Hubbard et al., 2006](#)). We used the volatile degassing model of [Iacono-Marziano et al. \(2012\)](#) implemented in the VESIcal Python package ([Iacovino et al., 2021](#)). Our calculations ([Figure 6c,d](#); Supplementary Figure B4) indicate that CO_2 and H_2O exsolve continuously but minimally during ascent through much of the crust, with the majority of exsolution occurring within the uppermost few hundred metres. Bubble growth during ascent exerts stress on the crystal framework, and high volatile contents increase bubble

number density, enhancing coalescence and promoting partial disaggregation. Our 3D vesicle analysis and degassing calculations, therefore, indicate that framework disaggregation occurred primarily within the uppermost levels of ascent, where bubbles grow and coalesce to volumes sufficient to disrupt the well-connected, equant to sub-equant plagioclase network. Bubbles already present at the final pressure of magma storage (~ 2.5 kbar) initially have little mechanical effect on the crystal framework, but contribute to stress as they expand during magma ascent.

Our observations are consistent with established models of shallow magma degassing (Degruyter et al., 2019), which identify three primary mechanisms for gas escape: (1) *bubble and crystal suspension* (e.g., Parmigiani et al., 2016) at very high melt fractions (green field in Figure 6d); (2) *volatile channel formation* (e.g., Parmigiani et al., 2011) at moderate melt and high crystal fractions (blue field); and (3) *capillary fracturing* (e.g., Parmigiani et al., 2017) at very low melt fractions, when melt pools are isolated (purple field). At the final storage depth, where the volatile fraction is negligible and the crystal fraction is expected to be high with isolated interstitial melt pockets, the mush is likely to degas predominantly by capillary fracturing (mechanism 3). Indeed, all Gígöldur samples (rock cores and thin sections) plot within this field (triangles in Figure 6) if vesicles are not included in the phase proportions. By the time the nodules reach the surface and have undergone significant degassing, the degassing mechanism has evolved to volatile channel formation (mechanism 2) in nearly all samples (diamonds in Figure 6). Taken together, the Gígöldur gabbroic nodules preserve the mesoscale structure of plagioclase-rich mushes in the Icelandic crust, owing to their rigid frameworks and efficient volatile escape pathways.

Given their preserved framework and connected volatile pathways, the density of the nodules remains a key factor controlling their ascent. Density calculations reveal that, even without volatile exsolution, the maximum density of the nodules remains close to neutral buoyancy; in all cases, the density contrast between nodules and carrier melt ranges from 0.18‰ to 1.13‰ (Table 1). Consequently, once detached from the mush horizon, these plagioclase-rich nodules could readily be entrained and transported by the carrier melt (Figure 7b). As nodules ascend, bubble nucleation, growth, and coalescence occur, which can lead to their disaggregation into individual crystals in the final ascent stages. However, we observe that many nodules have remained intact, as their mechanical integrity and vesicle connectivity provide structural resilience (Figure 7b). These findings indicate that the mesoscale structure of the subsurface mush horizon is a critical factor that determines whether a nodule will retain its structural integrity or disaggregate during ascent.

4.2. *What can we infer about mush structure and formation beneath Gígöldur?*

A key aim of this study is to decipher how the plagioclase-dominated framework of upper-crustal mushes is assembled by combining textural and chemical observations. Panjasawatwong et al. (1995) demonstrated that at crustal pressures, plagioclase with anorthite contents of 85–94 mol% can only crystallise from melts with CaO/Na₂O ratios of 10–15, Ca# values of 78–90 mol%, and Al# > 30 mol%. In contrast, the Gígöldur matrix glasses show systematically lower values for all these parameters (CaO/Na₂O = 4–7.6, Ca# = 68.8–80.8 mol%, Al# = 22.8–27.1 mol%; Table 2). Furthermore, (Lange et al., 2013) showed that the plagioclase macrophenocrysts with An > 85 mol% in plagioclase-ultraphyric basalts become

neutrally buoyant in their parental liquid only at pressures of 4–6 kbar. Taken together, these observations indicate that the high-An (An >85 mol%) plagioclase cores ([Figure 8](#)) within the gabbroic nodules could not have crystallised from the carrier melts sampled at Gígöldur (e.g., [Neave et al., 2014b](#)). Since we argue that disaggregation of gabbroic nodules feeds into plagioclase-ultrapphyric basalt crystal cargoes erupted in many settings, the high-An cores can reasonably be interpreted as recycled components inherited from deeper parts of the magmatic system and reworked into shallower levels where they acquired their rims ([Figure 2e-j](#)).

Our observations and calculations allow us to place some first-order constraints on the vapour content of Icelandic mushes in the crust. Considering the estimated maximum CO₂ concentrations of 1120–1350 ppm ([Supplementary Table 4](#)), calculations using the volatile saturation model of [Iacono-Marziano et al. \(2012\)](#), implemented in the VESIcal Python package ([Iacovino et al., 2021](#)), indicate that melts from Gígöldur became saturated with a CO₂-rich vapour at 1.97–2.80 kbar ([Table 2](#)). These pressures lie straddle magma storage pressures estimated by OPAM barometry ($\sim 2.45 \pm 1.14$ kbar; [Figure 5](#)). It is therefore likely that the mushes beneath Gígöldur contained low but non-zero volumes of exsolved CO₂-rich vapour at depth, as inferred for mushes beneath Bárðarbunga from seismic observations ([Hudson et al., 2017](#)).

We suggest that the Gígöldur magma was sourced from a mushy magma reservoir that formed through sill intrusion into the country rock, with mushes forming preferentially along sill boundaries ([MacLennan, 2019](#)). The intruding magma probably carried high-An plagioclase cores that originated in deeper or compositionally

distinct reservoirs and incorporated them into the present reservoir (Figure 7a; e.g., Halldorsson et al., 2008; Neave et al., 2014b). Within this mushy magma reservoir, recycled cores developed rim overgrowth while olivine and clinopyroxene co-crystallised (e.g., van Gerve et al., 2020). Density-driven segregation of these phases likely produced a plagioclase-rich roof and a mafic-rich base (Figure 7c). The zoning patterns observed between adjacent grains, which sometimes vary markedly (Figure 2e-j), indicate that the crystals did not share a single, uniform growth history and suggest that they were incorporated into clusters at different times and experienced differing degrees of (re-)equilibration with the resident melt (e.g., Bennett et al., 2019). Despite this variability, the compositional similarity between carrier and interstitial melts (Supplementary Figure B4) indicates that at least the final rim growth occurred in relatively homogeneous melts. Oscillatory zoning in several grains reflects non-steady-state growth driven by both dynamic processes, such as convection, melt replenishment, and interface kinetics (Ginibre et al., 2002), and thermodynamic factors, including variations in pressure, temperature, and melt composition during decompression and magma mixing (Ustunisik et al., 2014), although the preserved melt does not allow these processes to be constrained directly. Moreover, the variable zoning patterns in the clusters (Figure 3e-j) indicate that grains were incorporated at different times. Following these growth and zoning processes, at the final stage of mush assembly, textural observations (Figure 3a–d; Subbaraman et al., 2025b) indicate that olivine and clinopyroxene crystallised in interstitial positions relative to the plagioclase framework (Figure 7c). Outermost plagioclase rims grew in equilibrium with these interstitial melts, within analytical and model uncertainties (Figure 7c, Figure 8), which were multiply saturated with the mafic phases and plagioclase (Figure 5). Continued in-

terstitial crystallisation of mafic phases and rim overgrowth of plagioclase would have increased mush density toward neutral buoyancy, consistent with our density calculations (Table 1).

While more detailed geochemical and isotopic measurements would be required to test our model rigorously, our observations support the view that high-An plagioclase cores in our samples represent recycled, deeply crystallised components that were reworked into shallower cumulates during reservoir evolution. In this sense, the Gígöldur nodules provide a small-scale analogue of plagioclase-rich environments (e.g., anorthosites, troctolites) that have been proposed to contribute to plagioclase-ultraphyric basalt magmas in Iceland (e.g., Hansen and Grönvold, 2000; Neave et al., 2014b). Similar plagioclase-rich mush zones are observed beneath various mid-ocean ridge and ocean island settings, where they play a crucial role in the generation of basaltic magmas with comparable crystal cargoes (Lange et al., 2013). Studying such mushes enhances our understanding of how crystal cargoes in basaltic magmas are generated more generally, through processes such as mush entrainment and syn-eruptive disaggregation driven by volatile exsolution and degassing.

5. Conclusions

This study examines the structural integrity of nodules during ascent and the insights they provide into the structure and evolution of upper crustal (6–10 km) mushy magma reservoirs beneath Gígöldur. Gabbroic nodules preserve evidence of recycled high-An plagioclase cores and rim overgrowths, reflecting localised *in situ* modification within the mushy magma reservoir, and density-driven seg-

regation forming roof cumulates. Oscillatory zoning and variable rim patterns indicate that crystals experienced non-steady-state growth and were incorporated into clusters at different times. Final plagioclase rim overgrowth and interstitial mafic co-crystallisation likely marked the final stage of mush assembly. Compositional similarity between carrier and interstitial melts demonstrates that much of this final mush evolution occurred in relatively homogeneous melts.

Volatile saturation pressure estimates indicate that the melts hosting these nodules were likely volatile-saturated at their final storage conditions. Despite degassing-induced stresses, their rigid crystal frameworks maintained structural integrity, while highly connected vesicles provided efficient degassing pathways. Positive to neutral buoyancy likely facilitated nodule transport. Although bubble growth and coalescence may induce partial disaggregation, many nodules have remained intact, preserving primary mush textures. Poor bubble connectivity can lead to complete disaggregation, generating plagioclase-phyric crystal cargoes akin to those erupted in plagioclase-ultraphyric basalt lava.

In active crustal mush systems, the interplay of rigid crystal frameworks, melt connectivity, and vesicle networks governs whether mushes remain cohesive or disaggregate into crystal cargoes. The Gígöldur nodules provide a clear case study of these processes in an upper-crustal setting. Similar behaviours occur in other crustal systems: frameworks and interstitial melt have been observed to regulate mush disaggregation in samples from mid- to lower-crustal oceanic core complexes (e.g., [Boulanger et al., 2024](#)); in Icelandic systems, remobilisation has been shown to continuously supply macrocrysts to long-lasting eruptions (e.g., [Neave](#)

et al., 2017); in Tenerife OIBs, resorption, clustering, and partial disaggregation record complex histories (e.g., Horn et al., 2022); and in arc systems, recharge-driven remobilisation delivers crystal cargoes to eruptions (e.g., Cooper and Kent, 2014). Together, these observations support the three-phase (crystal–melt–vapour) nature of mush zones, with framework rigidity, melt connectivity, and volatile distribution controlling magma storage, remobilisation, and eruptive behaviour.

Acknowledgements

This publication results from work carried out under Trans-National Access action under the support of EXCITE - EC - HORIZON 2020 - INFRAIA 2020 Integrating Activities for Starting Communities under grant agreement N.101005611. Part of the EPMA data acquisition was conducted during the NERC Advanced Training Short Course in Quantitative X-ray Microanalysis in Earth and Environmental Sciences, funded by NERC grant NE/Y00373X/1. RS acknowledges support from the UoM FSE Dean's Doctoral Scholarship. DAN acknowledges support from NE/T011106/1. MEH acknowledges support from NERC grant NE/P002331/1. MP and BB acknowledge support from UKRI grant 4DVOLC (MR/V023985/1). RS thanks Lee Paul and David Oliver for their support with sample preparation. Finally, we thank Martin Mangler and an anonymous reviewer for their detailed and encouraging reviews, and Chiara Maria Petrone for editorial handling.

Declaration of AI-assisted technologies in the writing process

During the preparation of this manuscript, the author(s) used ChatGPT (OpenAI) to enhance the clarity and readability of the text. The author(s) reviewed, edited, and verified all content and take full responsibility for the published work.

Supplementary materials

The following supplementary materials are available in connection with this article:

1. MMC 1. Supplementary Information.pdf – Contains supplementary methods, figures, and tables referenced in the main text.
2. MMC 2. EPMA Setup + Sec Std.xlsx – EPMA instrument settings and chemical analyses of secondary standards.
3. MMC 3. EPMA Data - Glass + Minerals.xlsx – Chemical analyses of matrix glasses, melt inclusions, and median mineral data used for thermobarometry and density calculations.
4. MMC 4. Literature H₂O-CO₂.xlsx – Compilation of Icelandic literature data for H₂O and CO₂ used in this study.

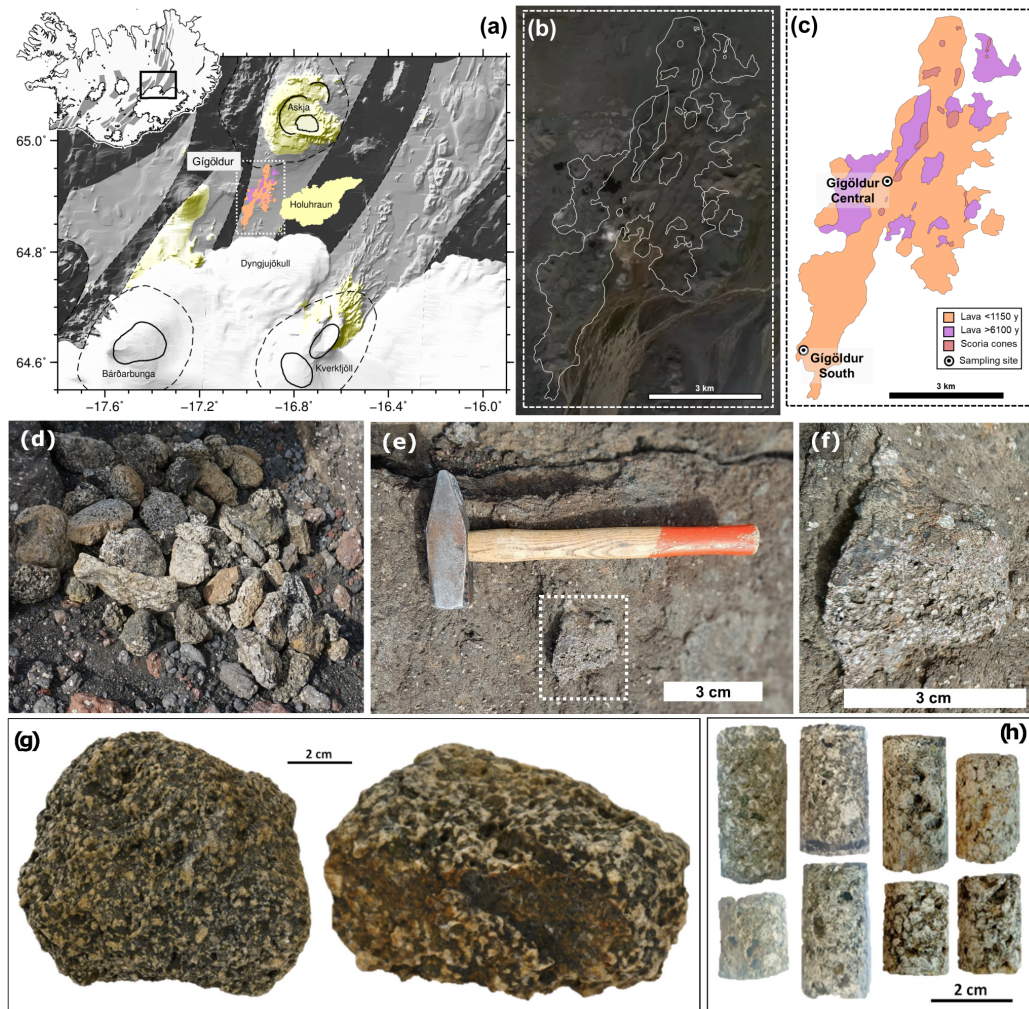


Figure 1: Geological context of gabbroic nodules. (a) Map of the highlands north of Vatnajökull showing Gígöldur, Holuhraun, Askja and Bárðarbunga. The inset shows Iceland with the neovolcanic zone highlighted, with the black bold rectangle corresponding to the highlands map. Within the highlands map, the white dashed rectangle marks the area expanded in panels (b)–(c). (b) Satellite image of Gígöldur and surrounding areas from [Google Earth Pro \(2025\)](#), with lithological boundaries after [Sigurgeirsson et al. \(2015\)](#). (c) Geological map of Gígöldur showing lava flows, scoria cones, and sampling locations (modified after [Sigurgeirsson et al. 2015](#)). (d) Field photograph illustrating the compositional and textural variability of nodules collected at Gígöldur Central. (e) Gabbroic nodule observed *in situ* within plagioclase-phyric scoriaceous agglutinates. (f) Enlarged view of the nodule shown in (e). (g) Nodules used in this study: GO19-01a.X (left) and GO19-02.X (right). (h) Rock cores extracted from the two nodules: GO19-01a.X (left) and GO19-02.X (right).

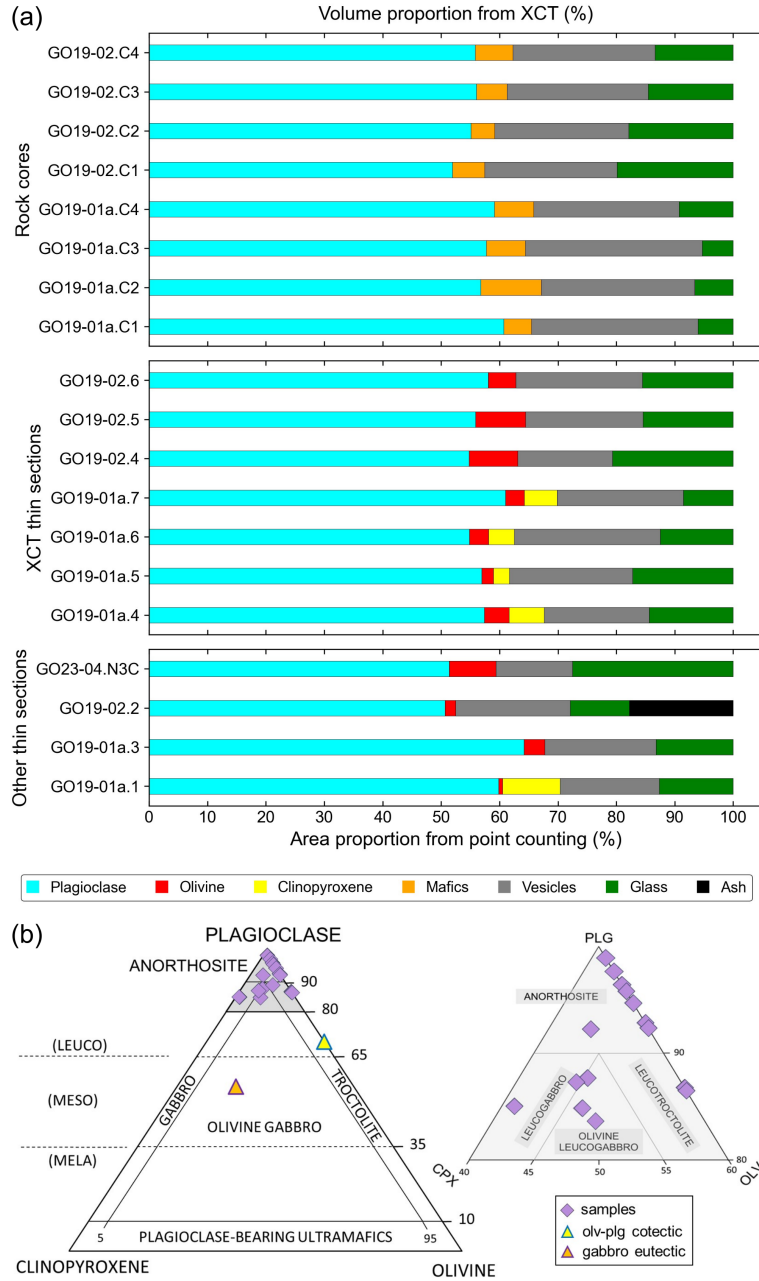


Figure 2: Phase proportions and classification of nodules. (a) Volume proportions from X-ray computed tomography (XCT) compared with area proportions from point counting. (b) IUGS gabbroic rock classification in plagioclase–olivine–clinopyroxene ternary diagrams. The main diagram shows compositional fields, the gabbro eutectic (orange triangle), and olivine–plagioclase cotectic (yellow triangle) compositions. The inset diagram enlarges the plagioclase-rich field (>80 vol%), illustrating the distribution of the studied thin sections.

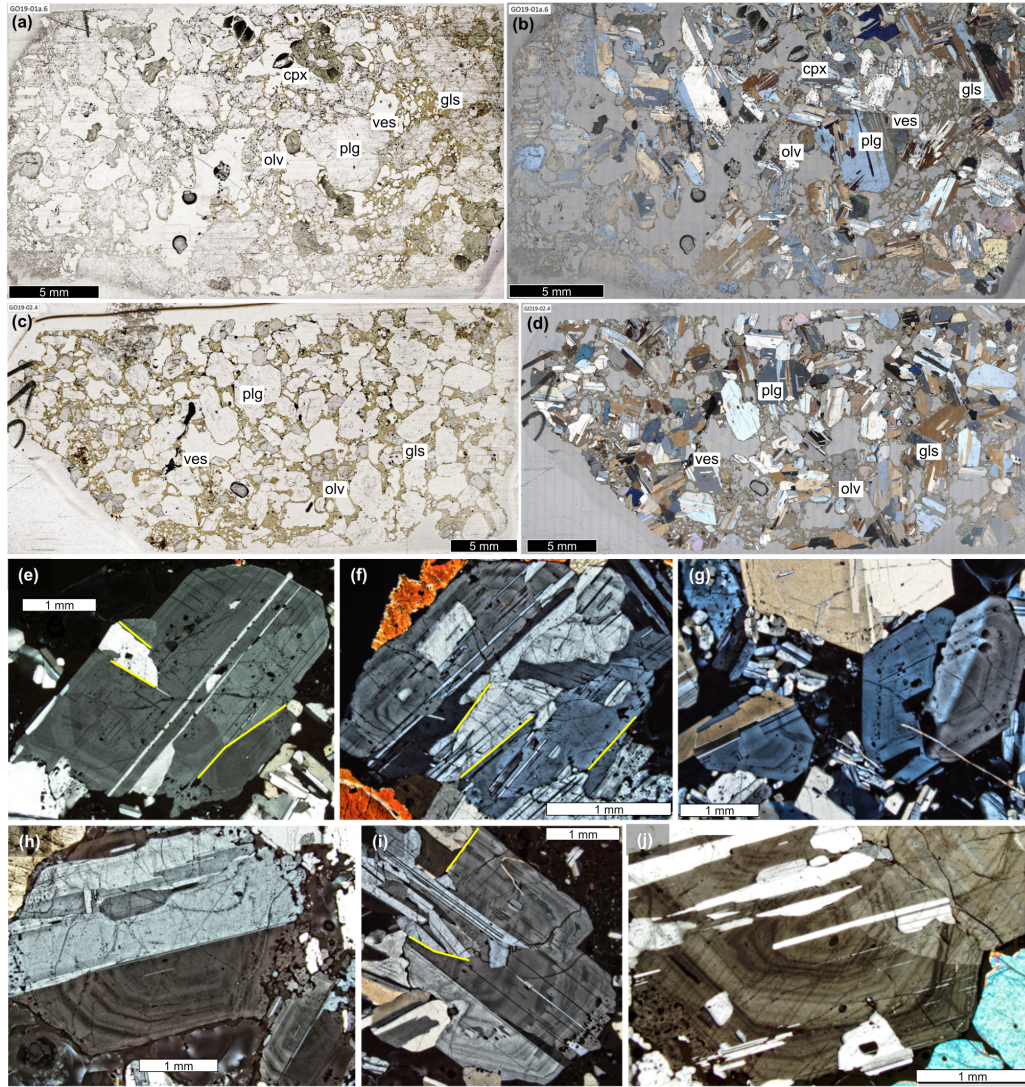


Figure 3: Petrography of gabbroic nodule thin sections. (a, c) Whole thin-section photomicrographs of GO19-01a.X and GO19-02.X in plane-polarised light (PPL). (b, d) Corresponding images in partial cross-polarised light (PXPL; polariser–analyser at 45°), with constituent phases indicated. The black scale bar represents 5 mm. (e–j) Photomicrographs of plagioclase grains from different samples highlighting complex zonation patterns with multiple bands of rims enclosing both individual crystals and crystal clusters. The yellow lines indicate examples of large contact areas between grains (see [subsection 4.1](#)). The white scale bar represents 1 mm.

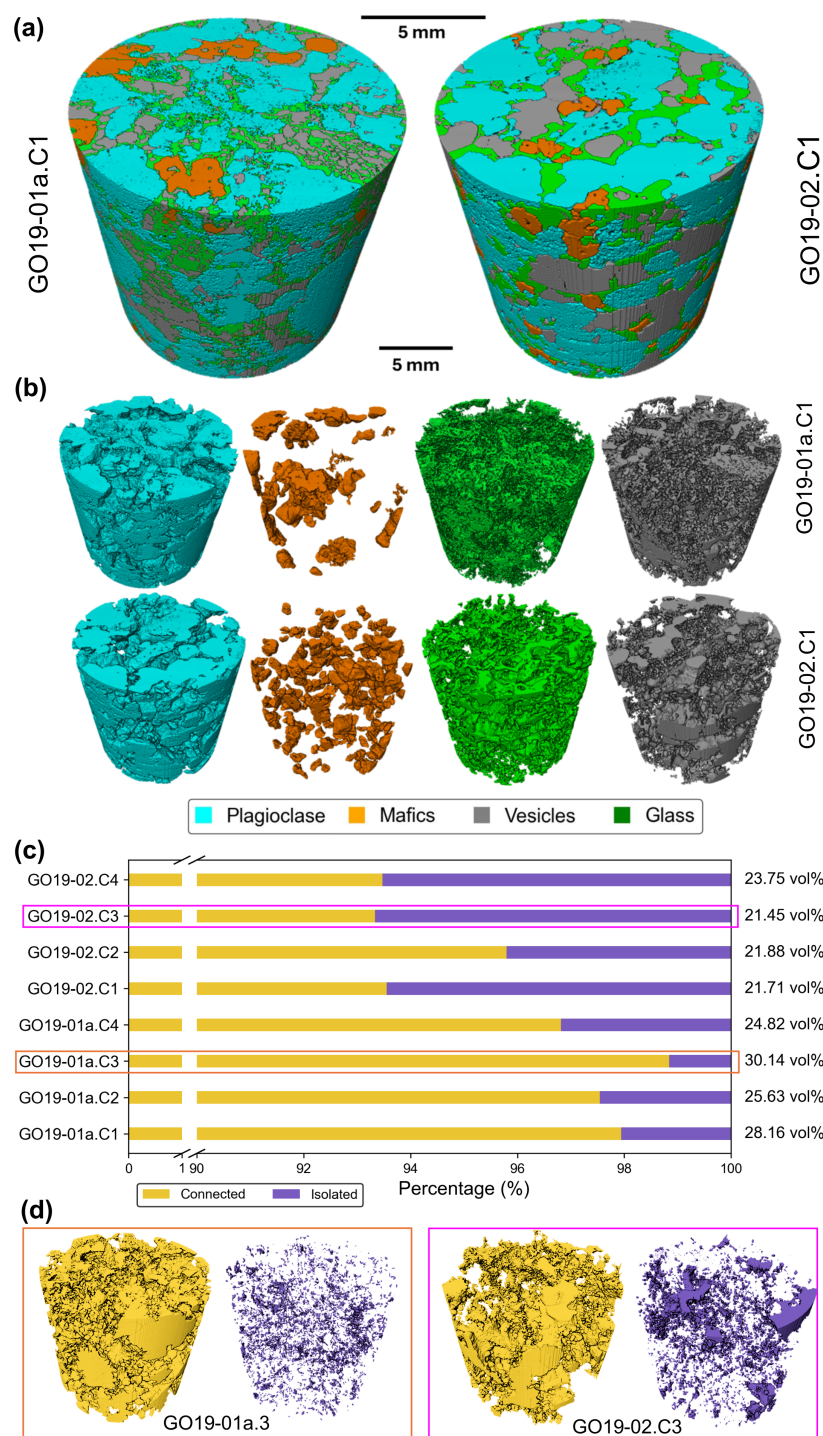


Figure 4: Results of XCT analysis. (a) Representative 3D reconstructions of whole cores with all phases combined (GO19-01a.C1 and GO19-02.C1). (b) Representative 3D reconstructions with individual phases distinguished (see legend for colour scheme). (c) Stacked bar chart showing vesicle connectivity categories (Connected and Isolated); vesicularity values for each sample are annotated on the right. The core with the highest proportion of Connected vesicles (GO19-01a.C3) is outlined in orange, and the core with the lowest proportion (GO19-02.C3) is outlined in magenta. (d) 3D reconstructions of Connected and Isolated vesicles for GO19-01a.C3 and GO19-02.C3, shown with orange and magenta outlines, respectively.

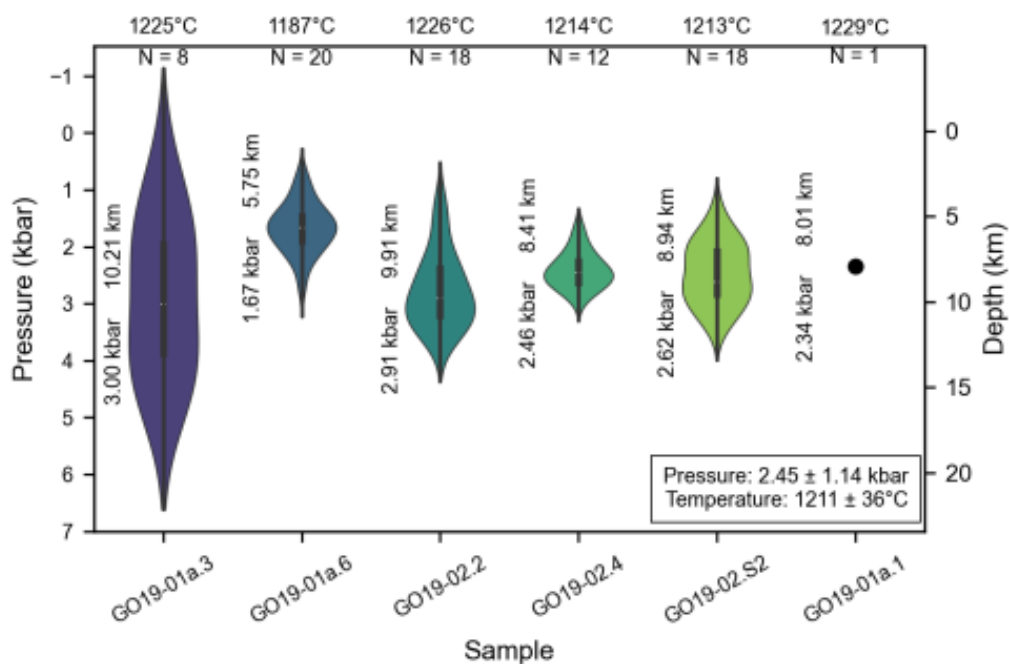


Figure 5: OPAM thermobarometry results for Gígöldur gabbroic nodules based on matrix glass compositions (Higgins and Stock, 2024). Violin plots show frequency distributions of calculated equilibrium pressures and equivalent storage depths for each sample. The number of glass analyses and median temperatures are annotated above each plot; median pressures and depths are indicated alongside each violin plot. Sample GO19-01a.1 yielded only one OPAM-saturated analysis and is shown as a single point rather than a distribution.

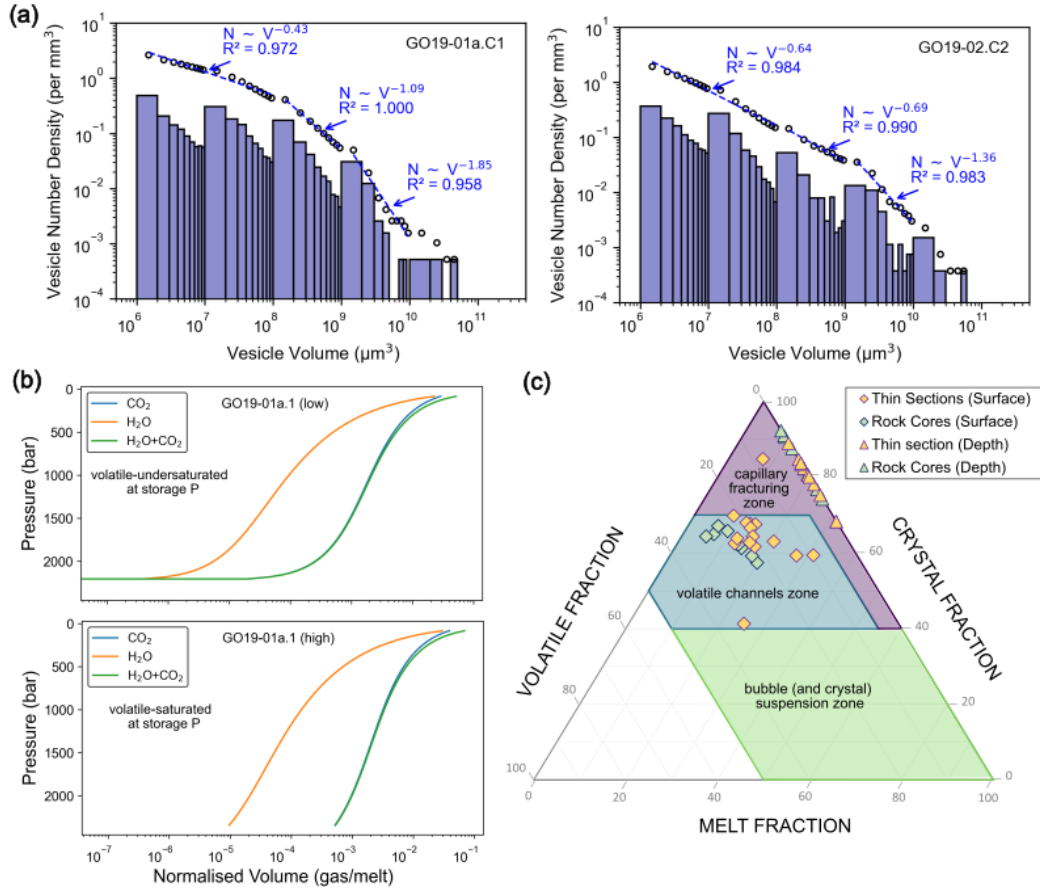


Figure 6: Vesicle growth dynamics and volatile degassing. (a) Cumulative (circles) and non-cumulative (bars) vesicle size distributions for representative cores from Batch I and Batch II, with fitted power-law trends; largest vesicles with exponents >1 . (b) Closed-system degassing profiles using the model of [Iacono-Marziano et al. \(2012\)](#), showing CO₂, H₂O, and H₂O+CO₂ from depth of final storage (~ 2.5 kbar) to ~ 84.5 bar (eruption beneath Icelandic glacial ice [Hubbard et al., 2006](#)). The upper panel illustrates a degassing melt initially undersaturated in volatiles, while the lower panel illustrates a degassing melt initially saturated in volatiles. Initial volatile contents and saturation pressures are provided in [Table 2](#). A full set of plots is provided in the supplementary material. (c) Ternary diagram of degassing regimes ([Degruyter et al., 2019](#)): (1) bubble/crystal suspension at high melt fractions (green), (2) volatile channels at moderate melt and high crystal fractions (blue), (3) capillary fracturing at very low melt fractions (purple). At final storage conditions, assuming negligible vesicle volumes, Gígöldur samples mostly plot in the capillary fracturing zone (triangles). At near-surface conduit conditions, the same samples plot in the volatile channels zone (diamonds).

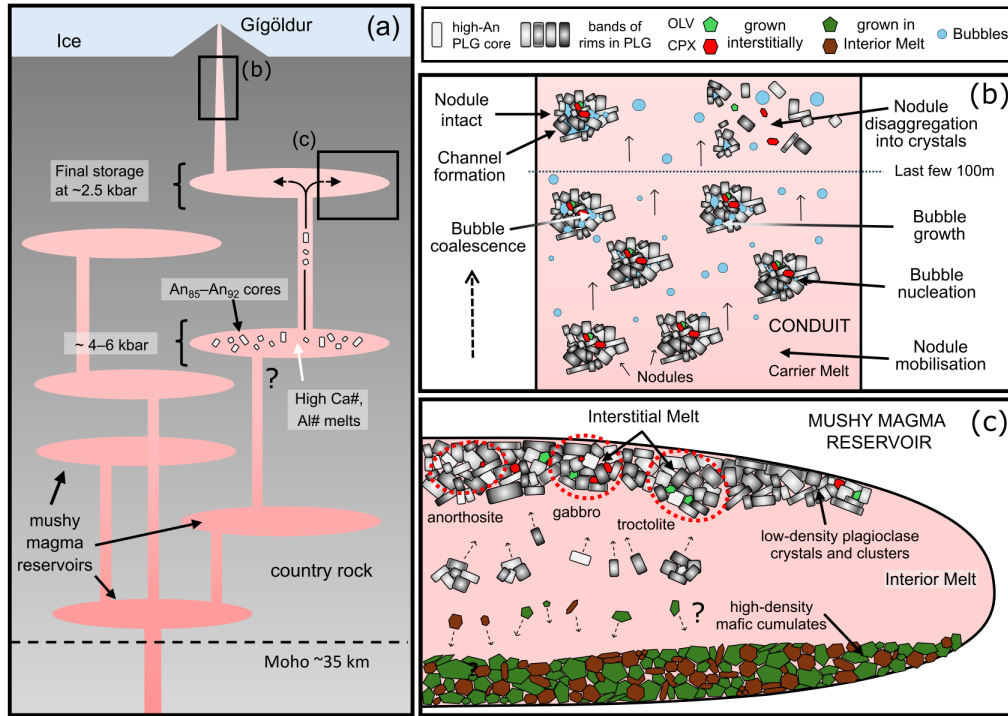


Figure 7: Conceptual model for the evolution, transport, and eruption of gabbroic nodules within the active mush system beneath Gígöldur. (a) Stacked sill-type transcrustal plumbing system, after MacLennan (2019). High-anorthite (An₈₅–An₉₂) plagioclase cores crystallise from high-Ca#, high-Al# melts in deep (~4–6 kbar) mushy magma reservoirs and are eventually transferred into a shallower reservoir at ~2.45 kbar. (b) Nodule behaviour during conduit ascent. Nodules are entrained by the carrier melt, while decompression drives bubble nucleation, growth, and coalescence. A combination of a strong crystal framework and interconnected bubble networks allows some nodules to remain intact, whereas the absence of either promotes their disaggregation into individual crystals in the upper conduit that feeds into the crystal cargo of plagioclase-ultraphyric basalts. (c) Organisation of the shallow mushy magma reservoir. Density-driven stratification produces a mafic cumulate base and a roof of recycled high-An cores modified by rim growth. Under conditions of multiple saturation, plagioclase, olivine, and clinopyroxene crystallise together from the interstitial melts. The resulting assemblages have gabbroic or troctolitic phase proportions within a plagioclase framework. The nodules erupted at the surface represent small-scale fragments of this plagioclase-dominated mush.

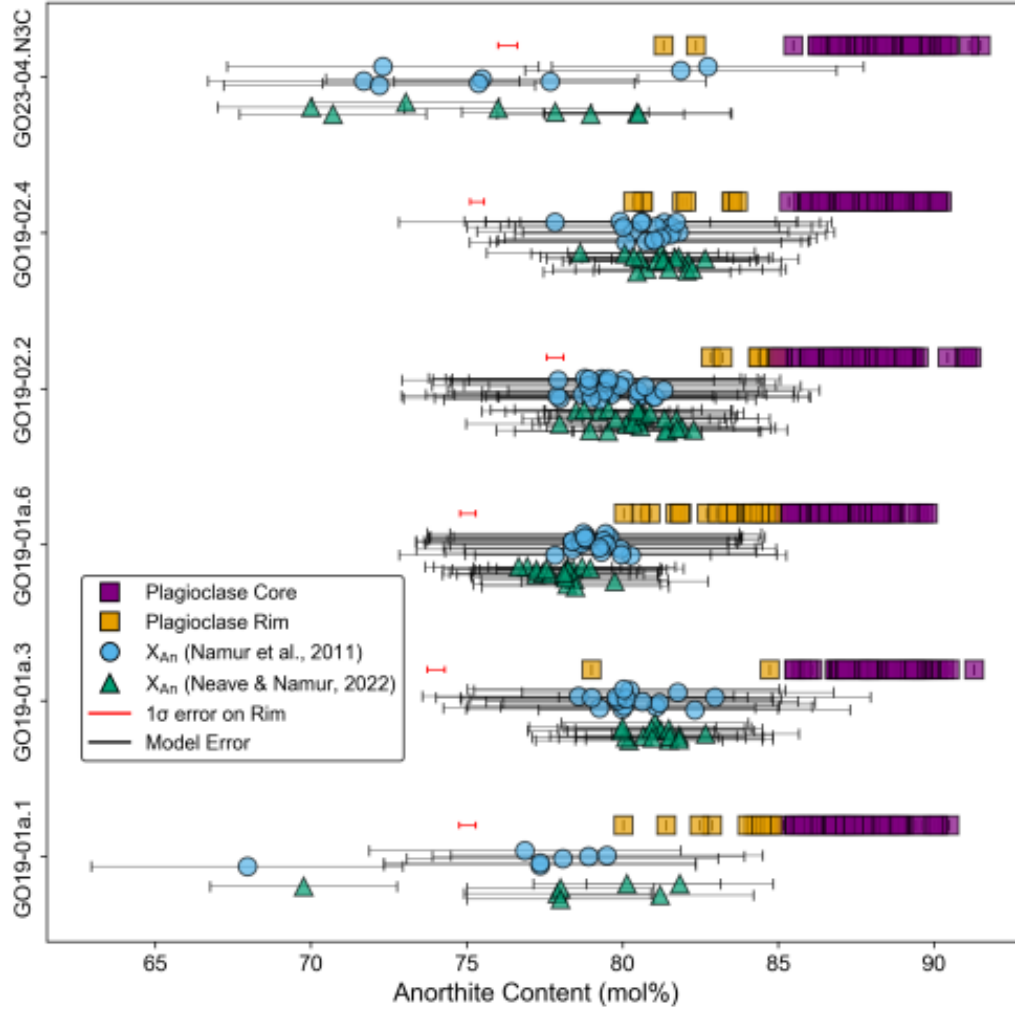


Figure 8: Anorthite contents of plagioclase cores and rims compared with equilibrium plagioclase calculations for the matrix glasses. Plagioclase cores (purple squares) are far from equilibrium with the surrounding matrix glass, indicating early crystallisation. Rims (orange squares) with the lowest An contents are in equilibrium with the surrounding matrix glass within model uncertainties. Equilibrium X_{An} of the matrix glass was calculated using two models: [Namur et al. \(2011\)](#) (blue circles) and [Neave and Namur \(2022\)](#) (green triangles). Horizontal red error bars indicate the mean uncertainty for rim compositions, while model error bars represent $\pm 3\text{--}5$ mol% uncertainty in the calculated equilibrium compositions.

Table 1: Phase densities, modal proportions, and bulk nodule densities for gabbroic nodules. Phase proportions are based on point counting, and densities are calculated at the final storage pressure and temperature. Nodule matrix glass is treated as interstitial melt (IM), while scoria matrix glass is treated as the carrier melt (CM). Abbreviations: PLG = plagioclase, OLV = olivine, CPX = clinopyroxene, IM = interstitial melt, CM = carrier melt.

Sample	Phase density (g/cm ³)				Vesicle-free proportions (%)				Final density (g/cm ³)		
	PLG	OLV	CPX	IM	PLG	OLV	CPX	IM	Nodule	CM	Δ_{rel}
GO19-01a.1	2.696	3.322	3.000	2.694	72.09	0.81	11.85	15.25	2.737	2.726	+0.40%
GO19-01a.3	2.701	3.253	-	2.734	79.23	4.42	-	16.35	2.731	2.736	-0.18%
GO19-01a.6	2.696	3.316	3.002	2.713	73.11	4.38	5.89	16.62	2.744	2.725	+0.69%
GO19-02.2	2.699	3.261	-	2.736	80.81	2.98	-	16.21	2.722	2.735	-0.48%
GO19-02.4	2.700	3.253	-	2.730	65.38	9.95	-	24.67	2.762	2.731	+1.13%
GO23-04.N3C	2.700	3.255	-	2.733	59.13	9.21	-	31.66	2.762	2.731	+1.13%

Table 2: Calculated melt volatile content and measured melt chemistry of nodule samples. P_{OPAM} and T_{OPAM} are calculated using OPAM thermobarometry. CO_2^{ll} and CO_2^{ul} are the lower (1020 ppm) and upper (1350 ppm) limits of the maximum CO_2 range calculated, respectively. P_{sat}^{ll} and P_{sat}^{ul} are volatile saturation pressures corresponding to mixed H_2O - CO_2 fluids with CO_2^{ll} and CO_2^{ul} , respectively. Ca# [$100 \times Ca / (Ca + Na)$], and Al# [$100 \times Al / (Al + Si)$] reflect melt chemistry relevant to the crystallisation of high-An plagioclase.

Sample	P_{OPAM} (kbar)	T_{OPAM} (°C)	H_2O (wt%)	CO_2^{ll} (ppm)	P_{sat}^{ll} (kbar)	CO_2^{ul} (ppm)	P_{sat}^{ul} (kbar)	CaO/Na ₂ O		Ca#		Al#	
								min	max	min	max	min	max
GO19-01a.1	2.34	1229	0.407	1020	2.22	1350	2.80	4.0	7.4	68.8	80.4	24.0	25.0
GO19-01a.3	3.00	1225	0.415	1020	2.05	1350	2.58	6.5	7.3	78.1	80.1	25.2	27.0
GO19-01a.6	1670	1187	0.398	1020	2.09	1350	2.64	5.6	7.0	75.4	79.3	24.8	26.3
GO19-02.2	2.91	1226	0.447	1020	1.97	1350	2.49	6.0	7.6	76.9	80.8	25.1	26.3
GO19-02.4	2.46	1214	0.432	1020	2.03	1350	2.56	6.2	7.5	77.5	80.5	25.4	26.4
GO23-04.N3C	2.45	1211	0.383	1020	2.06	1350	2.60	5.1	7.2	73.7	80.0	22.8	27.1

References

- Annen, C., Blundy, J.D., Sparks, R.S.J., 2005. The genesis of intermediate and silicic magmas in deep crustal hot zones. *Journal of Petrology* 47, 505–539. doi:<https://doi.org/10.1093/petrology/egi084>.
- Bacon, C.R., 1986. Magmatic inclusions in silicic and intermediate volcanic rocks. *Journal of Geophysical Research: Solid Earth* 91, 6091–6112. doi:[10.1029/jb091ib06p06091](https://doi.org/10.1029/jb091ib06p06091).
- Bai, L., Baker, D.R., Rivers, M., 2008. Experimental study of bubble growth in stromboli basalt melts at 1 atm. *Earth and Planetary Science Letters* 267, 533–547. doi:[10.1016/j.epsl.2007.11.063](https://doi.org/10.1016/j.epsl.2007.11.063).
- Bali, E., Hartley, M.E., Halldórsson, S.A., Gudfinnsson, G.H., Jakobsson, S., 2018. Melt inclusion constraints on volatile systematics and degassing history of the 2014–2015 holuhraun eruption, Iceland. *Contributions to Mineralogy and Petrology* 173. doi:[10.1007/s00410-017-1434-1](https://doi.org/10.1007/s00410-017-1434-1).
- Bamber, E.C., La Spina, G., Arzilli, F., Polacci, M., Mancini, L., de' Michieli Vitturi, M., Andronico, D., Corsaro, R.A., Burton, M.R., 2024. Outgassing behaviour during highly explosive basaltic eruptions. *Communications Earth and Environment* 5. doi:[10.1038/s43247-023-01182-w](https://doi.org/10.1038/s43247-023-01182-w).
- Bennett, E.N., Lissenberg, C.J., Cashman, K.V., 2019. The significance of plagioclase textures in mid-ocean ridge basalt (gakkel ridge, arctic ocean). *Contributions to Mineralogy and Petrology* 174. doi:[10.1007/s00410-019-1587-1](https://doi.org/10.1007/s00410-019-1587-1).
- Bergantz, G.W., Schleicher, J.M., Burgisser, A., 2015. Open-system dynamics

- and mixing in magma mushes. *Nature Geoscience* 8, 793–796. doi:[10.1038/ngeo2534](https://doi.org/10.1038/ngeo2534).
- Berman, R.G., 1988. Internally-consistent thermodynamic data for minerals in the system Na₂O-K₂O-CaO-MgO-FeO-Fe₂O₃-Al₂O₃-SiO₂-TiO₂-H₂O-CO₂. *Journal of Petrology* 29, 445–522. doi:[10.1093/petrology/29.2.445](https://doi.org/10.1093/petrology/29.2.445).
- Bonechi, B., Bamber, E.C., Polacci, M., Arzilli, F., La Spina, G., Biagioli, E., Romero, J.E., Hazemann, J.L., Brooker, R., Atwood, R., Burton, M., 2025. Linking eruptive style with pore network geometry in tephritic/basanitic tephra from the 2021 tajogaite eruption (canary islands, spain). *Bulletin of Volcanology* 87. doi:[10.1007/s00445-025-01833-0](https://doi.org/10.1007/s00445-025-01833-0).
- Boulanger, M., Godard, M., Ildefonse, B., Bakouche, M., 2024. Petrological evidence for prominent melt-mush reactions during slow-spreading oceanic accretion. *Geochemistry, Geophysics, Geosystems* 25. URL: <http://dx.doi.org/10.1029/2023GC011409>, doi:[10.1029/2023gc011409](https://doi.org/10.1029/2023gc011409).
- Candela, P.A., 1991. Physics of aqueous phase evolution in plutonic environments. *American Mineralogist* 76, 1081–1091.
- Cashman, K.V., Mangan, M.T., 2014. A century of studying effusive eruptions in Hawaii. doi:[10.3133/pp18019](https://doi.org/10.3133/pp18019).
- Cashman, K.V., Sparks, R.S.J., Blundy, J.D., 2017. Vertically extensive and unstable magmatic systems: A unified view of igneous processes. *Science* 355. URL: <http://dx.doi.org/10.1126/science.aag3055>, doi:[10.1126/science.aag3055](https://doi.org/10.1126/science.aag3055).

- Chamberlain, K.J., Barclay, J., Preece, K.J., Brown, R.J., Davidson, J.P., 2019. Lower crustal heterogeneity and fractional crystallization control evolution of small-volume magma batches at ocean island volcanoes (ascension island, south atlantic). *Journal of Petrology* 60, 1489–1522. doi:[10.1093/petrology/egz037](https://doi.org/10.1093/petrology/egz037).
- Colombier, M., Scheu, B., Wadsworth, F.B., Cronin, S., Vasseur, J., Dobson, K.J., Hess, K., Tost, M., Yilmaz, T.I., Cimorelli, C., Brenna, M., Ruthensteiner, B., Dingwell, D.B., 2018. Vesiculation and quenching during surtseyan eruptions at hunga tonga-hunga ha'apai volcano, tonga. *Journal of Geophysical Research: Solid Earth* 123, 3762–3779. doi:[10.1029/2017jb015357](https://doi.org/10.1029/2017jb015357).
- Coombs, M.L., Eichelberger, J.C., Rutherford, M.J., 2003. Experimental and textural constraints on mafic enclave formation in volcanic rocks. *Journal of Volcanology and Geothermal Research* 119, 125–144. doi:[10.1016/s0377-0273\(02\)00309-8](https://doi.org/10.1016/s0377-0273(02)00309-8).
- Cooper, K.M., Kent, A.J.R., 2014. Rapid remobilization of magmatic crystals kept in cold storage. *Nature* 506, 480–483. doi:[10.1038/nature12991](https://doi.org/10.1038/nature12991).
- Degruyter, W., Parmigiani, A., Huber, C., Bachmann, O., 2019. How do volatiles escape their shallow magmatic hearth? *Philosophical Transactions of the Royal Society A: Mathematical, Physical and Engineering Sciences* 377, 20180017. doi:[10.1098/rsta.2018.0017](https://doi.org/10.1098/rsta.2018.0017).
- Edmonds, M., Cashman, K.V., Holness, M., Jackson, M., 2019. Architecture and dynamics of magma reservoirs. *Philosophical Transactions of the Royal Society A: Mathematical, Physical and Engineering Sciences* 377, 20180298.

URL: <http://dx.doi.org/10.1098/rsta.2018.0298>, doi:<https://doi.org/10.1098/rsta.2018.0298>.

Edmonds, M., Wallace, P.J., 2017. Volatiles and exsolved vapor in volcanic systems. *Elements* 13, 29–34. doi:[10.2113/gselements.13.1.29](https://doi.org/10.2113/gselements.13.1.29).

Gaonac’h, H., Lovejoy, S., Stix, J., Scherzter, D., 1996. A scaling growth model for bubbles in basaltic lava flows. *Earth and Planetary Science Letters* 139, 395–409. doi:[10.1016/0012-821x\(96\)00039-8](https://doi.org/10.1016/0012-821x(96)00039-8).

van Gerve, T.D., Neave, D.A., Almeev, R.R., Holtz, F., Namur, O., 2020. Zoned crystal records of transcrustal magma transport, storage and differentiation: Insights from the shatsky rise oceanic plateau. *Journal of Petrology* 61. doi:[10.1093/petrology/egaa080](https://doi.org/10.1093/petrology/egaa080).

Ginibre, C., Wörner, G., Kronz, A., 2002. Growth kinetics of plagioclase in igneous rocks: constraints from natural zoning patterns. *Contributions to Mineralogy and Petrology* 143, 300–315.

Google Earth Pro, 2025. Satellite imagery of gígöldur, iceland. <https://earth.google.com/>. Data provided by Maxar Technologies, CNES/Airbus.

Halldorsson, S.A., Oskarsson, N., Gronvold, K., Sigurdsson, G., Sverrisdottir, G., Steinthorsson, S., 2008. Isotopic-heterogeneity of the thjorsa lava—implications for mantle sources and crustal processes within the eastern rift zone, iceland. *Chemical Geology* 255, 305–316. doi:[10.1016/j.chemgeo.2008.06.050](https://doi.org/10.1016/j.chemgeo.2008.06.050).

Hansen, H., Grönvold, K., 2000. Plagioclase ultraphyric basalts in iceland: the

- mush of the rift. *Journal of Volcanology and Geothermal Research* 98, 1–32. doi:[10.1016/s0377-0273\(99\)00189-4](https://doi.org/10.1016/s0377-0273(99)00189-4).
- Hauri, E.H., MacLennan, J., McKenzie, D., Gronvold, K., Oskarsson, N., Shimizu, N., 2017. CO₂ content beneath northern Iceland and the variability of mantle carbon. *Geology* 46, 55–58. doi:[10.1130/g39413.1](https://doi.org/10.1130/g39413.1).
- Higgins, O., Stock, M.J., 2024. A New Calibration of the OPAM Thermobarometer for Anhydrous and Hydrous Mafic Systems. *Journal of Petrology* 65. doi:[10.1093/petrology/egae043](https://doi.org/10.1093/petrology/egae043).
- Holness, M.B., 2018. Melt segregation from silicic crystal mushes: a critical appraisal of possible mechanisms and their microstructural record. *Contributions to Mineralogy and Petrology* 173. doi:[10.1007/s00410-018-1465-2](https://doi.org/10.1007/s00410-018-1465-2).
- Holness, M.B., Anderson, A.T., Martin, V.M., MacLennan, J., Passmore, E., Schwindinger, K., 2007. Textures in partially solidified crystalline nodules: a window into the pore structure of slowly cooled mafic intrusions. *Journal of Petrology* 48, 1243–1264. doi:[10.1093/petrology/egm016](https://doi.org/10.1093/petrology/egm016).
- Holness, M.B., Humphreys, M.C.S., Sides, R., Helz, R.T., Tegner, C., 2012. Toward an understanding of disequilibrium dihedral angles in mafic rocks. *Journal of Geophysical Research: Solid Earth* 117. doi:[10.1029/2011jb008902](https://doi.org/10.1029/2011jb008902).
- Holness, M.B., Stock, M.J., Geist, D., 2019. Magma chambers versus mush zones: constraining the architecture of sub-volcanic plumbing systems from microstructural analysis of crystalline enclaves. *Philosophical Transactions of the Royal Society A: Mathematical, Physical and Engineering Sciences* 377, 20180006. doi:[10.1098/rsta.2018.0006](https://doi.org/10.1098/rsta.2018.0006).

- Holness, M.B., Vukmanovic, Z., Mariani, E., 2017. Assessing the role of compaction in the formation of adcumulates: a microstructural perspective. *Journal of Petrology* 58, 643–673. doi:[10.1093/petrology/egx037](https://doi.org/10.1093/petrology/egx037).
- Horn, E.L., Taylor, R.N., Gernon, T.M., Stock, M.J., Farley, E.M.R., 2022. Composition and petrology of a mush-bearing magma reservoir beneath tenerife. *Journal of Petrology* 63. doi:[10.1093/petrology/egac095](https://doi.org/10.1093/petrology/egac095).
- Hubbard, A., Sugden, D., Dugmore, A., Norddahl, H., Pétursson, H.G., 2006. A modelling insight into the icelandic last glacial maximum ice sheet. *Quaternary Science Reviews* 25, 2283–2296. doi:[10.1016/j.quascirev.2006.04.001](https://doi.org/10.1016/j.quascirev.2006.04.001).
- Hudson, T.S., White, R.S., Greenfield, T., Ágústsdóttir, T., Brisbourne, A., Green, R.G., 2017. Deep crustal melt plumbing of bárðarbunga volcano, iceland. *Geophysical Research Letters* 44, 8785–8794. doi:[10.1002/2017gl074749](https://doi.org/10.1002/2017gl074749).
- Humphreys, M.C.S., Namur, O., Bohrsen, W.A., Bouilhol, P., Cooper, G.F., Cooper, K.M., Huber, C., Lissenberg, C.J., Morgado, E., Spera, F.J., 2025. Crystal mush processes and crustal magmatism. *Nature Reviews Earth and Environment* 6, 401–416. doi:[10.1038/s43017-025-00682-x](https://doi.org/10.1038/s43017-025-00682-x).
- Iacono-Marziano, G., Morizet, Y., Le Trong, E., Gaillard, F., 2012. New experimental data and semi-empirical parameterization of h₂o–co₂ solubility in mafic melts. *Geochimica et Cosmochimica Acta* 97, 1–23. doi:[10.1016/j.gca.2012.08.035](https://doi.org/10.1016/j.gca.2012.08.035).
- Iacovino, K., Matthews, S., Wieser, P.E., Moore, G.M., Bégué, F., 2021. Vesical part i: An open-source thermodynamic model engine for mixed volatile

- (h₂o-co₂) solubility in silicate melts. *Earth and Space Science* 8. doi:[10.1029/2020ea001584](https://doi.org/10.1029/2020ea001584).
- Klug, C., Cashman, K.V., 1994. Vesiculation of may 18, 1980, mount st. helens magma. *Geology* 22, 468–472. doi:[10.1130/0091-7613\(1994\)022<0468:VOMMSH>2.3.CO;2](https://doi.org/10.1130/0091-7613(1994)022<0468:VOMMSH>2.3.CO;2).
- Klug, C., Cashman, K.V., 1996. Permeability development in vesiculating magmas: implications for fragmentation. *Bulletin of Volcanology* 58, 87–100. doi:[10.1007/s004450050128](https://doi.org/10.1007/s004450050128).
- Lange, A.E., Nielsen, R.L., Tepley, F.J., Kent, A.J.R., 2013. The petrogenesis of plagioclase-phyric basalts at mid-ocean ridges. *Geochemistry, Geophysics, Geosystems* 14, 3282–3296. doi:[10.1002/ggge.20207](https://doi.org/10.1002/ggge.20207).
- Lange, R.L., Carmichael, I.S.E., 1990. Chapter 2. Thermodynamic properties of silicate liquids with emphasis on density, thermal expansion and compressibility. De Gruyter. p. 25–64. doi:[10.1515/9781501508769-006](https://doi.org/10.1515/9781501508769-006).
- MacLennan, J., 2019. Mafic tiers and transient mushes: evidence from iceland. *Philosophical Transactions of the Royal Society A: Mathematical, Physical and Engineering Sciences* 377, 20180021. doi:[10.1098/rsta.2018.0021](https://doi.org/10.1098/rsta.2018.0021).
- Martin, V., Pyle, D., Holness, M., 2006. The role of crystal frameworks in the preservation of enclaves during magma mixing. *Earth and Planetary Science Letters* 248, 787–799. doi:[10.1016/j.epsl.2006.06.030](https://doi.org/10.1016/j.epsl.2006.06.030).
- Namur, O., Charlier, B., Toplis, M.J., Vander Auwera, J., 2011. Prediction of plagioclase-melt equilibria in anhydrous silicate melts at 1-atm. *Contributions to Mineralogy and Petrology* 163, 133–150. doi:[10.1007/s00410-011-0662-z](https://doi.org/10.1007/s00410-011-0662-z).

- Neave, D.A., Buisman, I., MacLennan, J., 2017. Continuous mush disaggregation during the long-lasting laki fissure eruption, iceland. *American Mineralogist* 102, 2007–2021. doi:[10.2138/am-2017-6015ccby](https://doi.org/10.2138/am-2017-6015ccby).
- Neave, D.A., MacLennan, J., Edmonds, M., Thordarson, T., 2014a. Melt mixing causes negative correlation of trace element enrichment and CO₂ content prior to an Icelandic eruption. *Earth and Planetary Science Letters* 400, 272–283. doi:[10.1016/j.epsl.2014.05.050](https://doi.org/10.1016/j.epsl.2014.05.050).
- Neave, D.A., MacLennan, J., Hartley, M.E., Edmonds, M., Thordarson, T., 2014b. Crystal storage and transfer in basaltic systems: the skuggafjöll eruption, iceland. *Journal of Petrology* 55, 2311–2346. doi:[10.1093/petrology/egu058](https://doi.org/10.1093/petrology/egu058).
- Neave, D.A., Namur, O., 2022. Plagioclase archives of depleted melts in the oceanic crust. *Geology* 50, 848–852. doi:[10.1130/g49840.1](https://doi.org/10.1130/g49840.1).
- O’Driscoll, B., Emeleus, C.H., Donaldson, C.H., Daly, J.S., 2010. Cr-spinel seam petrogenesis in the rum layered suite, nw scotland: Cumulate assimilation and in situ crystallization in a deforming crystal mush. *Journal of Petrology* 51, 1171–1201. doi:[10.1093/petrology/egq013](https://doi.org/10.1093/petrology/egq013).
- Panjasawatwong, Y., Danyushevsky, L.V., Crawford, A.J., Harris, K.L., 1995. An experimental study of the effects of melt composition on plagioclase-melt equilibria at 5 and 10 kbar: implications for the origin of magmatic high-an plagioclase. *Contributions to Mineralogy and Petrology* 118, 420–432. doi:[10.1007/s004100050024](https://doi.org/10.1007/s004100050024).
- Parmigiani, A., Degruyter, W., Leclaire, S., Huber, C., Bachmann, O., 2017. The

- mechanics of shallow magma reservoir outgassing. *Geochemistry, Geophysics, Geosystems* 18, 2887–2905. doi:[10.1002/2017gc006912](https://doi.org/10.1002/2017gc006912).
- Parmigiani, A., Faroughi, S., Huber, C., Bachmann, O., Su, Y., 2016. Bubble accumulation and its role in the evolution of magma reservoirs in the upper crust. *Nature* 532, 492–495. doi:[10.1038/nature17401](https://doi.org/10.1038/nature17401).
- Parmigiani, A., Huber, C., Bachmann, O., Chopard, B., 2011. Pore-scale mass and reactant transport in multiphase porous media flows. *Journal of Fluid Mechanics* 686, 40–76. doi:[10.1017/jfm.2011.268](https://doi.org/10.1017/jfm.2011.268).
- Paulatto, M., Moorkamp, M., Hautmann, S., Hooft, E., Morgan, J.V., Sparks, R.S.J., 2019. Vertically extensive magma reservoir revealed from joint inversion and quantitative interpretation of seismic and gravity data. *Journal of Geophysical Research: Solid Earth* 124, 11170–11191. doi:[10.1029/2019jb018476](https://doi.org/10.1029/2019jb018476).
- Polacci, M., Baker, D.R., La Rue, A., Mancini, L., Allard, P., 2012. Degassing behaviour of vesiculated basaltic magmas: an example from ambrym volcano, vanuatu arc. *Journal of Volcanology and Geothermal Research* 233–234, 55–64. doi:[10.1016/j.jvolgeores.2012.04.019](https://doi.org/10.1016/j.jvolgeores.2012.04.019).
- Polacci, M., Baker, D.R., Mancini, L., Favretto, S., Hill, R.J., 2009. Vesiculation in magmas from stromboli and implications for normal strombolian activity and paroxysmal explosions in basaltic systems. *Journal of Geophysical Research: Solid Earth* 114. doi:[10.1029/2008jb005672](https://doi.org/10.1029/2008jb005672).
- Proussevitch, A., Ketcham, R., Carlson, W., Sahagian, D., 1998. Preliminary results of x-ray ct analysis of hawaiian vesicular basalts. *Eos* 79, 360.

- Roduit, N., 2008. JMicroVision: Image analysis toolbox for measuring and quantifying components of high-definition images. <https://jmicrovision.github.io>.
- Shea, T., Houghton, B.F., Gurioli, L., Cashman, K.V., Hammer, J.E., Hobden, B.J., 2010. Textural studies of vesicles in volcanic rocks: An integrated methodology. *Journal of Volcanology and Geothermal Research* 190, 271–289. doi:[10.1016/j.jvolgeores.2009.12.003](https://doi.org/10.1016/j.jvolgeores.2009.12.003).
- Sigurgeirsson, M.A., Árni Hjartarson, Kaldal, I., mundsson, K.S., ur Garð ar Kristinsson, S., Víkingsson, S., 2015. Geological map of the northern volcanic zone, iceland. southern part.
- Sparks, R.S.J., Brazier, S., 1982. New evidence for degassing processes during explosive eruptions. *Nature* 295, 218–220. doi:[10.1038/295218a0](https://doi.org/10.1038/295218a0).
- Sparks, R.S.J., Cashman, K.V., 2017. Dynamic magma systems: Implications for forecasting volcanic activity. *Elements* 13, 35–40. doi:[10.2113/gselements.13.1.35](https://doi.org/10.2113/gselements.13.1.35).
- Subbaraman, R., 2025. Density_calc. doi:[10.5281/zenodo.16943747](https://doi.org/10.5281/zenodo.16943747).
- Subbaraman, R., Hartley, M., Neave, D.A., 2025a. Thin section scans of gabbro nodules, scoria, plagioclase-phyric basalt, hyaloclastite from gígöldur, central iceland. Figshare. doi:[10.48420/28435859.v1](https://doi.org/10.48420/28435859.v1).
- Subbaraman, R., Hartley, M., Polacci, M., Bonechi, B., Pappalardo, L., Buono, G., Neave, D.A., 2025b. X-ray computed micro-tomography (xct) 3d reconstructions of icelandic gabbro nodules. Figshare. doi:[10.48420/28431773.v1](https://doi.org/10.48420/28431773.v1).

- Toramaru, A., 2006. Bnd (bubble number density) decompression rate meter for explosive volcanic eruptions. *Journal of Volcanology and Geothermal Research* 154, 303–316. doi:[10.1016/j.jvolgeores.2006.03.027](https://doi.org/10.1016/j.jvolgeores.2006.03.027).
- Tukey, J.W., 1977. *Exploratory Data Analysis*. Addison-Wesley Pub. Co., Reading, MA.
- Ustunisik, G., Kilinc, A., Nielsen, R.L., 2014. New insights into the processes controlling compositional zoning in plagioclase. *Lithos* 200–201, 80–93. doi:[10.1016/j.lithos.2014.03.021](https://doi.org/10.1016/j.lithos.2014.03.021).